



## INPR-Connector: Interlocking negative Poisson's ratio connectors design for deployable energy absorption structures

Wenpeng Xu <sup>a</sup>, Mengyu Zhang <sup>a</sup>, Hao Xu <sup>a,b</sup>, Menglin Yu <sup>c</sup>, Liuchao Jin <sup>d</sup>,<sup>\*</sup>  
Xiaoya Zhai <sup>e</sup>, Jingchao Jiang <sup>f</sup>

<sup>a</sup> School of Computer Science Technology, Henan Polytechnic University, Jiaozuo, 454003, China

<sup>b</sup> School of Computer Science and Technology, Shandong University, Qingdao, 266237, China

<sup>c</sup> School of Mechanical and Power Engineering, Henan Polytechnic University, Jiaozuo, Henan 454000, China

<sup>d</sup> Department of Mechanical and Automation Engineering, The Chinese University of Hong Kong, Hong Kong, China

<sup>e</sup> School of Mathematical Sciences, University of Science and Technology of China, Hefei, 230026, China

<sup>f</sup> Department of Engineering, University of Exeter, Exeter, EX4 4QF, UK

### ARTICLE INFO

**Keywords:**

Deployable structures  
Negative Poisson's ratio structure  
Energy absorption  
Interlocking connector  
Origami structure

### ABSTRACT

Deployable energy absorption structures are widely utilized in aircraft landing gear, seismic support systems, and transport vessels due to their unique designs that significantly improve energy absorption capacity. However, current studies encounter challenges related to insufficient connection strength and suboptimal energy absorption performance. To address these issues, this paper proposed an interlocking negative Poisson's ratio connector (INPR-Connector) with expansion capabilities and geometric interlocking functions, aimed at enhancing both connectivity and energy absorption. We developed two types of structures: complete structure filling (CSF) and intermediate part filling (IPF), and experimentally validated the superior connection performance and energy absorption capabilities of unit cell-generated structures under various geometric configurations. Moreover, the proposed connection structure was integrated with a rigid plate to create an expandable, bistable origami structure embedded INPR-Connector. When the load is applied, the hinge can store energy through deformation, converting the applied load into tensile forces within the horizontal flexible hinges. This structure can also recover its original shape after multiple cycles of compression, demonstrating excellent load-bearing capacity. Both numerical simulations and physical experiments confirm the effectiveness and feasibility of the designed connection structure within expandable configurations. The results indicate that this structure not only possesses adjustable energy absorption capabilities but also significantly enhances impact resistance.

### 1. Introduction

A deployable energy absorption structure [1] is a system capable of being compactly folded and subsequently unfolded for use. It is designed to absorb and dissipate energy when subjected to external forces, such as impacts [2,3], vibrations [4], or compressive loads [5]. The energy absorption and dissipation are primarily achieved through the structure's geometric configuration and material properties. These structures find extensive applications in lightweight design [6,7], collision safety [8,9], and aerospace engineering [10–14]. Examples include foldable honeycomb structures [15–18], origami configurations [19–22], and foldable composite support structures [23–26].

The growing demand for deployable energy absorption structures has made designing more stable configurations with enhanced energy absorption capacity an important research focus. Especially in

aerospace, deployable structures such as satellite solar panels, antennas, and detection equipment play a crucial role in absorbing external impacts, ensuring stable system operation, and reducing vibration effects during deployment [27–29]. As a result, increasing attention has been dedicated to understanding and optimizing the performance of these structures. For example, Wang et al. [30] introduced thin plates into thin-walled tubes inspired by Miura Origami, proposing a novel pre-folded tube design. Wo et al. [31] developed a deployable origami tube, utilizing the LOCTITE® adhesive system to bond the zipper tube to an acrylic plate. Wu et al. [32] studied the impact performance of bistable composite shells during collisions with space debris, developing a stretchable hybrid composite material composed of carbon–carbon, carbon–Kevlar, Kevlar–Kevlar, and graphene-

\* Corresponding authors.

E-mail addresses: [liuchao.jin@link.cuhk.edu.hk](mailto:liuchao.jin@link.cuhk.edu.hk) (L. Jin), [xiaoyazhai@ustc.edu.cn](mailto:xiaoyazhai@ustc.edu.cn) (X. Zhai).

reinforced polyurethane elastomers, which significantly improved energy absorption. However, the fabrication of each layer in this design was achieved through adhesive bonding. Deleo et al. [33] designed a foldable, rigid structure using carbon fiber-reinforced polymer composites, relying primarily on adhesive bonding techniques. Notably, none of these studies have addressed the role of connecting structures within their designs.

Realizing effective connections is essential, as these connections significantly influence the overall mechanical properties of the structure. Currently, various methods have been proposed to facilitate the connection of different structures. Ye et al. [34] proposed a wrapper-based multi-material 3D printing strategy, where rigid panels are wrapped in stretchable soft parts to effectively prevent interlayer separation. However, differences in deformation between soft and hard structures can lead to stress concentration under large tension, and thin cladding may fracture. Chueh et al. [35,36] reported combining polymer–metal and ceramic multi-material parts using the laser powder bed fusion technique. Wagner et al. [37] used fused deposition modeling (FDM) and inkjet printing to print aramid fibers and polyamide hinges, which can be folded approximately  $10^6$  times. However, the direct application of these methods to deployable energy absorption structures has not yet been demonstrated. Hunter et al. [38] introduced a framework for designing unidirectional and bidirectional hinges, using viscoelastic materials combined with rigid plates to form deployable structures. Faber et al. [39] fabricated a biomimetic spring origami that enables rigid origami folding and variable stiffness by printing a rigid face (acrylonitrile butadiene styrene — ABS) onto a rubbery substrate (thermoplastic polyurethane — TPU). However, weak interface bonding between materials with differing properties can result in delamination, causing structural failure at the interface during folding and unfolding. Further developments have explored direct multi-material printing [40–42], yet most of these structures still rely on the adhesive force of adjacent layers and are prone to disconnection under relatively small loads. Recently, more stable connection structures have been proposed. Yang et al. [43] developed an interlocking assembly strategy to design and fabricate 3D double-V hierarchical lattices with multiple materials. Ituarte et al. [44] explored the design and fabrication of functionally graded structures using multi-material binder jetting. Brischetto et al. [45] employed the sandwich method to prepare a plate with acrylonitrile butadiene styrene as the outer layer and polylactic acid as the core. Saldivar et al. [46] fabricated a functional gradient connection structure based on triply periodic minimal surfaces (TPMS), colloidal triple helix, and randomly distributed particles, which offered strong mechanical properties but was limited by manufacturing equipment. Porter et al. [47] designed a bionic hinge inspired by fish skin armors, while Stano et al. [48] developed adhesion mechanisms inspired by biological joints, including spiral and linear shapes. Other approaches incorporate multiple materials through path planning [49, 50]. Although these structures demonstrate good mechanical properties, most lack flexibility, limiting their applicability in deployable systems. Additionally, many studies focus on connecting two structures, often overlooking the impact of the connection on overall performance when integrating multiple structural elements.

For energy absorption and shock mitigation, the negative Poisson's ratio (NPR) structure has emerged as a promising solution [51–53]. As a type of mechanical metamaterial [54], NPR structures offer unique dilatability, allowing them to reduce material usage while maintaining robust mechanical properties. Inspired by natural cellular configurations, NPR structures have been widely studied [55]. For instance, Lim [56] designed a mechanical metamaterial based on rotating trapezoids and triangles, achieving adjustable positive and NPR. Wang et al. [57] developed a bi-directional re-entrant anti-tetrachiral NPR structure to meet the deformation requirements of a wing. Feng et al. [58] proposed a concave four-arc honeycomb structure based on the star-shaped honeycomb, modifying the straight rods into curved ones while retaining the re-entrant angle. Yang et al. [59] developed

a novel 3D star-shaped NPR element and composite structure. Qin et al. [60] proposed two axisymmetric tetrachiral honeycomb structures. Li et al. [61] proposed a novel corrugated star-shaped honeycomb hybrid core sandwich structure and investigated its impact response. Wang and Fu [62] and Fu et al. [63] introduced an innovative hardened sandwich doubly curved shell with an arcuate, growing honeycomb core. NPR properties have also been integrated into origami structures [64,65], where folding kinematics allow for adjustable Poisson's ratios. Despite the potential of NPR structures in energy absorption applications, few studies have explored their integration with connection structures, limiting their broader application in multi-material deployable systems.

To address these challenges, this paper introduces novel approaches for developing integrated deployable structures with adjustable mechanical properties by utilizing multi-material additive manufacturing. The focus lies on the critical issue of hard and soft interface connections in multi-material 3D printing. We propose an INPR-Connector, which combines the traditional mortise-and-tenon design with an NPR configuration. First, the NPR unit is generated through solid modeling, where a set of parameters controls its shape and dimensions. Two connection structures with varying fill ratios are created by applying array and Boolean intersection operations to the unit cells: the complete structure filling (CSF) and the intermediate part filling (IPF). To ensure manufacturability, we evaluate the minimum printable wall thickness and packing fraction of the unit cell, defining the packing resolution within the design domain. Subsequently, a series of simulations and physical tests are conducted to analyze the geometric and mechanical properties of the INPR-Connector under different form factors and volume fractions. Finally, an origami-inspired deployable structure, featuring embedded NPR elements, is constructed by integrating the designed connection structure with rigid plates. Experimental results validate the feasibility and effectiveness of the proposed connection structure.

## 2. Geometric configuration and property analysis of NPR unit cells

### 2.1. The geometrical configuration of the orthogonal elliptical unit cell

The NPR unit cell used in this paper is an orthogonal elliptical hole structure [66,67], as shown in Fig. 1(a). We have synthesized previous research and found that this porous structure exhibits superior structural stability and energy absorption capability compared to other NPR structures, such as the concave hexagonal structure, double-arrow unit cell structure, and star-shaped unit cell structure [68–70]. The orthogonal elliptical structure was selected primarily for its ability to significantly enhance energy absorption performance and maintain excellent mechanical properties during large deformations. By tuning the aspect ratio of the ellipse, the deformation behavior of the structure can be precisely controlled, optimizing its mechanical response under various loading conditions. The orthogonal elliptical shape provides superior structural stability, better compression resistance, and enhanced energy absorption capacity. While other NPR structures may excel in certain aspects, they are prone to stress concentration under large deformations or complex loading, particularly at junctions or seams. In contrast, the orthogonal elliptical geometry effectively mitigates these issues, enabling superior toughness and extended service life under extreme loads. Here,  $W$  denotes the length of the structure comprising multiple single cells within a defined design domain, while  $L$  represents the length of a single cell. The ratio  $W/L$  specifies the number of small cells along the horizontal and vertical axes, respectively. Additionally,  $\rho$  is the volume fraction,  $t$  is the wall thickness of the orthogonal elliptical unit,  $a$  is the length of the ellipse's major axis,  $b$  is the length of the ellipse's minor axis, and the geometric factor  $m = a/b$  determines the overall shape, as it is the ratio between the major and minor axes. The area of a single cell can be calculated using the following equation:

$$S_c = L^2 - \pi ab. \quad (1)$$

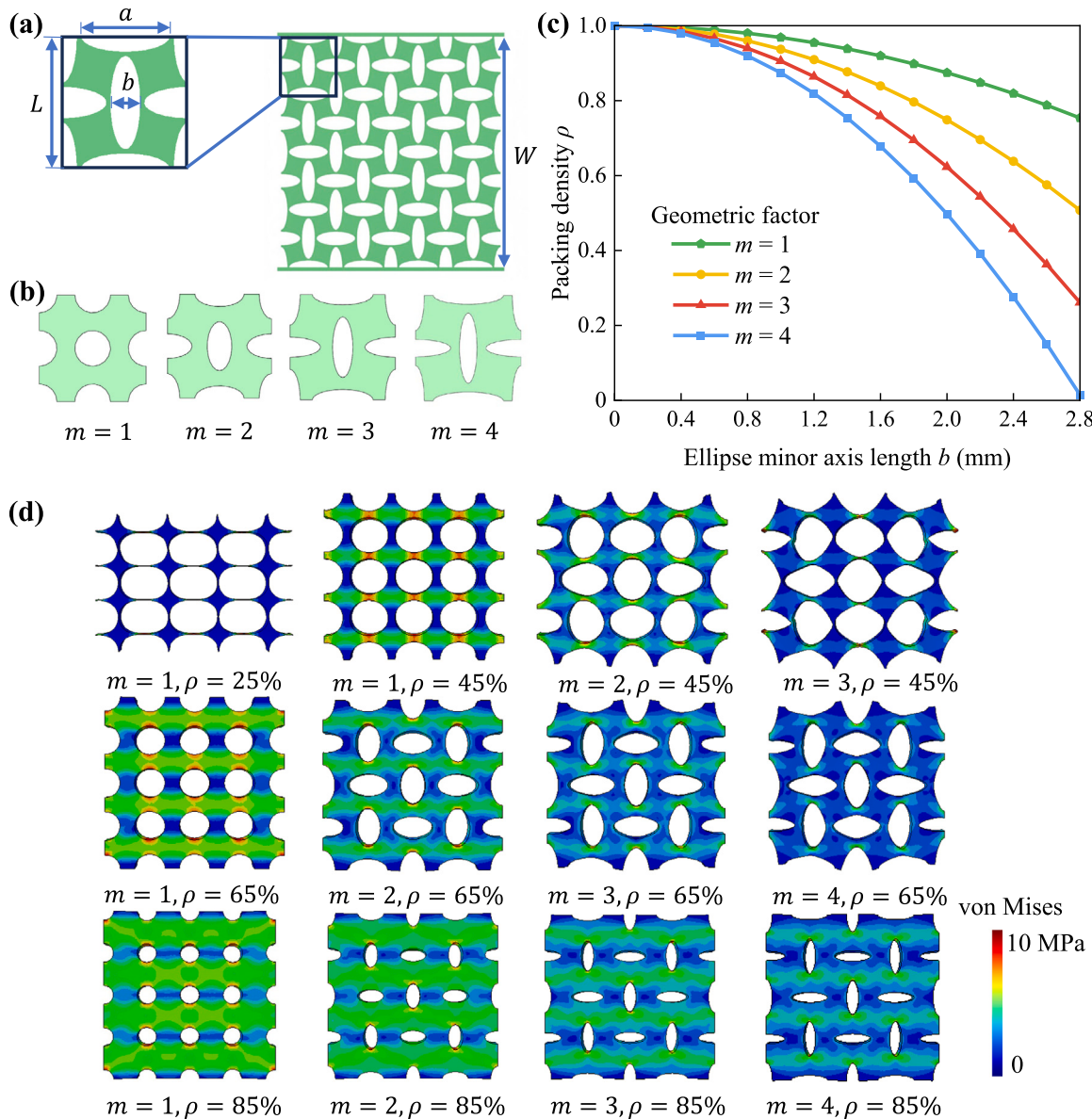


**Fig. 1.** Design and properties of orthogonal elliptical hole structure. (a) Schematic of the geometric parameters of a single cell. (b) The filling fraction is the four monoids with different geometric factors at 65%. (c) Range of effective volume fractions under different geometric factor monoids. (d) Stress distribution of four structures with volume fractions of 25%, 45%, 65%, and 85%.

## 2.2. Mechanical properties of NPR single cell

In this study, the volume fraction of the orthogonal elliptical hole NPR structure is defined as the ratio of the area of a single cell to the area of its planar bounding box. Given a fixed length \$L\$ for a single cell, the cell's volume fraction under various geometric factors \$m\$ can be adjusted by modifying the parameter values. Since \$m = a/b\$, controlling the volume fraction of the unit cell can be achieved by varying the length of the minor axis \$b\$, as illustrated in Fig. 1(b). The volume fraction of the NPR structure is given by the equation:

$$\rho = 1 - \pi m b^2 / L^2. \quad (2)$$

However, an excessively small volume fraction can lead to structural failure, such as fracture phenomena, which prevent the porous structure from forming a continuous whole, thereby complicating additive manufacturing processes. Conversely, an overly large volume fraction can also result in manufacturing difficulties. For example, when the voids within the porous structure become too small relative to the

nozzle diameter, the holes in the printed sample will disappear entirely. To mitigate these issues, it is essential to calculate the effective volume fraction of the generated porous structures with various geometric factors \$m\$. The design and filling constraints of the unit cell are determined by the inequalities \$a + b < L\$ and \$m = a/b\$, as follows:

$$(m+1)b < L. \quad (3)$$

Therefore, the range of effective volume fraction is deduced as follows:

$$1 - \pi m / (m+1)^2 < \rho \leq 1. \quad (4)$$

Within this effective range, 15 sets of \$b\$-value samples are uniformly selected for four structural cells with different long-to-short axis ratios. Based on these samples, porous structural cells with varying volume fractions are generated. The sampled minor axis length \$b\$ is then fitted to the volume fraction to establish a relationship. Fig. 1(c) shows the dependence of the effective volume fraction of the generated monoids on the parameter \$b\$ for the four geometric factors. The results indicate that when the geometric factor \$m = 1\$, the unit cell has the largest effective volume fraction range. Conversely, when \$m = 4\$, the range of

**Table 1**

Maximum displacement of the structure under four different geometric factors with volume fractions of 25%, 45%, 65%, and 85%.

$\rho$	Maximum displacement (mm)			
	$m = 1$	$m = 2$	$m = 3$	$m = 4$
25%	8.664	–	–	–
45%	1.568	2.646	4.633	–
65%	0.865	1.170	1.764	2.692
85%	0.541	0.589	0.695	0.821

effective volume fractions for a single cell is minimized. These findings underscore the design limitations associated with both high and low volume fractions in porous structure design.

### 2.3. Finite element analysis of unit cell physical properties

The mechanical properties of porous structures are significantly influenced by their geometric configuration. To evaluate and compare the mechanical properties of unit cells with various shapes, we conduct finite element analysis on cells with four different geometric factors  $m$ . Specifically, unit cells of dimensions  $10\text{ mm} \times 10\text{ mm} \times 2\text{ mm}$  are designed with volume fractions of 25%, 45%, 65%, and 85%. Each unit cell is arranged in a  $20\text{ mm} \times 20\text{ mm} \times 2\text{ mm}$  region, periodically filling the area with monoids of identical shape and volume fraction. Two monoids are filled in both the  $x$  and  $y$  directions within each design domain, while the  $z$  dimension remain constant.

To predict the deformation of the orthogonal elliptical unit, we performed finite element simulations using the ABAQUS software package (V6.22-1, Dassault Systèmes Simulia, USA). The nonlinear finite element analysis was conducted using the hyperelastic Mooney-Rivlin model with a strain energy density function  $W = C_{10}(I_1 - 3) + C_{01}(I_2 - 3) + \frac{1}{D_1}(J - 1)^2$ . The material coefficients were set to  $C_{10} = 0.78\text{ MPa}$  and  $C_{01} = 0.19\text{ MPa}$ . A mesh with 8-node linear hexahedral elements (C3D8RH) was used, with a mesh size of 0.3. The left boundary of the model was fully fixed, and a uniform load was applied on the right side. Due to the small size of the model and the thinner wall thickness at  $m = 1$  and  $\rho = 25\%$  (which results from the smaller volume fraction), the final minimum load was set to 4.5 N.

Fig. 1(d) displays the stress distribution of porous structures with a 45% volume fraction across different geometric factors  $m$ . When the shape is circular ( $m = 1$ ), the porous structure exhibits significant stress concentration. However, porous structures with geometric factors  $m = 2, 3, 4$  demonstrate favorable NPR properties, with more uniform stress distributions.

Table 1 presents the maximum displacement observed for each geometric factor under finite element analysis. Null values are indicated by “–” in cases where effective fill scores are not achievable at certain volume fractions. It is evident that  $m = 2, 3, 4$  exhibit null values at 25% and 45% fill fractions due to the limited effective range for these geometric factors. Notably, at the same volume fraction, unit cells with  $m = 4$  yield the largest displacement, suggesting superior NPR performance. For instance, with a volume fraction of 65%, the maximum displacement for  $m = 4$  reaches 2.692 mm, compared to 0.865 mm for  $m = 1$ , indicating that higher geometric factors enhance mechanical performance under comparable conditions. At a volume fraction of 45%,  $m = 3$  exhibits the best mechanical characteristics.

NPR materials undergo substantial lateral deformation when stretched, which enhances their capacity for energy dispersion and absorption. Let  $\nu$  denote Poisson's ratio, and  $\varepsilon_1$  and  $\varepsilon_2$  represent strains in the vertical and horizontal directions, respectively. The following equation is used to calculate Poisson's ratio:

$$\nu = -\varepsilon_1/\varepsilon_2. \quad (5)$$

Both computational and physical property analyses reveal that, without considering manufacturability, unit cells with a geometric factor of  $m = 4$  exhibit the most favorable NPR performance. In contrast, monoids with  $m = 1$  lack the NPR properties desirable for these applications.

## 3. Design of INPR-Connector

This section presents the design methodology and manufacturability of the INPR-Connector, developed through multi-material additive manufacturing. First, we outline the design workflow for the INPR-Connector. Subsequently, a manufacturability analysis is conducted for the proposed CSF and IPF structures. In parallel, the unit cell's filling resolution is determined based on the minimum printable accuracy and volume fraction. Finally, experimental verification is performed to assess the effectiveness of the designed structures.

### 3.1. Design process of connection structure

The design workflow for the INPR-Connector using multi-material additive manufacturing is depicted in Fig. 2(a). The process begins with the creation of a 3D model of an interlocking structure, which serves as the foundation of the design. Next, the prototype for the INPR-Connector is formed by incorporating unit cells with NPR effects. Through Boolean operations on this prototype and the initial model, the final configuration of the INPR-Connector is established, offering two variations: the CSF and IPF. With the interconnected structure in place, FEA is applied to evaluate its mechanical properties. Following simulation, the structure is manufactured using TPU, a flexible material that enhances its adaptability. Lastly, the manufactured flexible connection structure is attached to a rigid plate to create the Rigid-Soft-Rigid (RSR) configuration, completing the design and yielding the final sample.

### 3.2. Model structure design and size definition

The fill pattern significantly influences the performance and quality of 3D-printed objects. By optimizing fill density, range, and pattern, a balance between printing efficiency and material consumption can be achieved. In light of these considerations, the design of the INPR-Connector, illustrated in Fig. 2(a), includes two configurations — CSF and IPF — to assess tensile properties. In this design, the IPF only materializes at the joint sections, while the rest remains consistent with the CSF.

Two specific sizes are defined for testing purposes, as shown in Fig. 2(c), with a volume fraction of 65% and a geometric factor of 3. The unit cell measures  $10\text{ mm} \times 10\text{ mm} \times 2\text{ mm}$ , with the middle section comprising a  $2 \times 2$  arrangement of cells stacked longitudinally in sets of four. The first configuration,  $40 \times 15$ , features a lock head arranged horizontally and laterally with three cells, while the second configuration,  $40 \times 20$ , arranges the lock head laterally with four cells. This arrangement allows for precise control of the interlocking angle by adjusting the unit cell count in the joint section, while preserving the primary structural characteristics.

The odd and even units are arranged distinctly at the joints, which results in variations in the interlocking angles. This design approach not only enhances mechanical performance but also offers substantial flexibility. The model's shape and size can be customized, allowing for size adjustments to accommodate different connection requirements as needed.

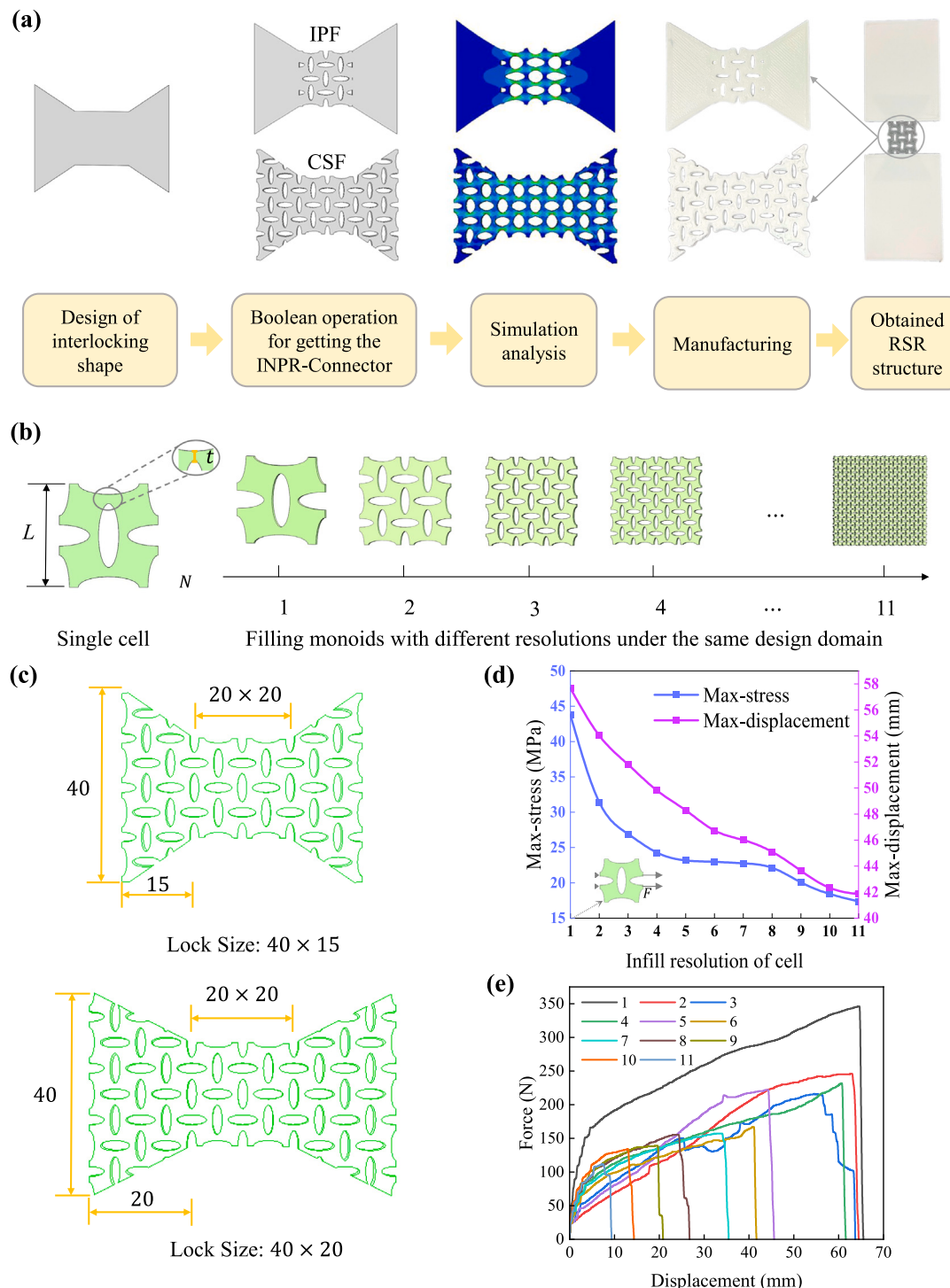


**Fig. 2.** Design for INPR-Connector. (a) INPR-Connector design flow. (b) Monomials with a geometric factor of 3 filled with different resolutions under the same design domain. (c) INPR-Connector under CSF with two size definitions. (d) Maximum stress and maximum displacement of NPr structures at different packing resolutions within the same domain. (e) Monoidal Uniaxial Tensile Force–Displacement Curves for a Fixed Packing Domain with Packing Resolutions Ranging from 1 to 11.

### 3.3. Manufacturability

In practical design, it is essential to consider the minimum accuracy of 3D printing to ensure that unit cell dimensions fall within a manufacturable range. First, the packing resolution of the unit cell within the design domain must be determined, ensuring that the minimum wall thickness is above the printer's minimum printable accuracy. If the fill resolution is too high, the wall thickness of the unit cell may fall

below the minimum printable threshold, resulting in fabrication failure. When defining the design domain size and unit cell volume fraction, wall thickness decreases as volume fraction increases. The effective minimum unit size  $L$  can be calculated using the following formula:

$$L = \frac{2t}{1 - (m + 1)\sqrt{(1 - \rho)/\pi m}}, \quad (6)$$

where  $t$  is the wall thickness between two adjacent ellipses.

The number of cells within the same region is constrained by the minimum printable wall thickness between adjacent ellipses. The limiting factor of cell size is expressed by Eq. (7). Under a fixed geometric factor  $m$ , the cell size is restricted by the structural volume fraction. Specifically, when the area and volume fraction are fixed, the wall thickness  $t$  between the elliptical holes decreases as the geometric factor  $m$  increases. This relationship limits the cell size, as the wall thickness cannot fall below the minimum printable threshold. The calculation process is described as follows:

$$t = \frac{L \left( 1 - (m+1)\sqrt{(1-\rho)/\pi m} \right)}{2} \quad (7)$$

**Fig. 2(b)** illustrates a single cell with a volume fraction of 60%, showing the packing of monoids at varying resolutions within the same design domain. Monoids with a geometric factor of 3 are demonstrated for packing resolutions from  $1 \times 1$  to  $11 \times 11$  within a  $50 \text{ mm} \times 50 \text{ mm} \times 2 \text{ mm}$  domain. As packing resolution increases, the wall thickness of the NPR structure decreases, approaching the limit of minimum fabrication accuracy.

Assuming a minimum manufacturing accuracy of 0.4 mm, the minimum printable wall thickness for a unit cell is also 0.4 mm. Based on the relationship between volume fraction, minimum printable wall thickness, and the geometric factor  $m$ , the minimum side length  $L$  of the unit cell is approximately 4.55 mm.

Packing resolution impacts not only the wall thickness of unit cells but also the mechanical properties of NPR structures. To explore the relationship between fill resolution and structural performance, finite element analysis is used to simulate mechanical properties at various fill resolutions, as shown in **Fig. 2(b)**. With the model's left boundary fully fixed and a uniform load of 100 N applied to the right side, **Fig. 2(d)** presents a line chart of simulation results, displaying variations in maximum stress (blue) and maximum displacement (purple) with changes in packing resolution. Results indicate that both maximum stress and maximum displacement decrease as packing resolution increases. However, high packing resolution can also lead to greater fabrication challenges. Therefore, selecting an appropriate packing resolution is critical to balancing mechanical properties and the manufacturability of NPR structures.

To verify the simulation results, uniaxial tensile tests were conducted on structures with varying resolutions. The experimental results are presented in **Fig. 2(e)**, and they demonstrate strong alignment with the simulation data, confirming the accuracy and reliability of the simulations.

#### 4. Mechanical properties verification and fabrication of RSR specimens

The algorithms for generating the proposed connection structures are implemented in C++ and executed on a laptop equipped with a 12th Gen Intel(R) Core(TM) i5-1240P CPU @ 1.70 GHz and 16 GB of RAM. All simulation experiments are conducted using ABAQUS software. Hyperelastic parameters are analyzed using the Mooney–Rivlin method for nonlinear finite element analysis, with  $C_{10} = 0.78 \text{ MPa}$  and  $C_{01} = 0.19 \text{ MPa}$ , and meshed using eight-node linear hexahedral elements (C3D8RH). All mockups are fabricated with a SNAPMAKER J1s high-speed IDEX 3D printer, utilizing a dual nozzle configuration. The nozzle diameter is  $w_n = 0.4 \text{ mm}$ , with a PLA printing speed of 105 mm/s at a nozzle temperature of 215 °C. The TPU printing speed is 25 mm/s at a nozzle temperature of 220 °C, using Ultimaker PLA and Ultimaker TPU95 A materials.

#### 4.1. Comparison of RSR connectors

This section compares traditional interlocking connection structures — U-Shape, T-Shape, and Trapezoid — as shown in **Fig. 3(a)**. Uniaxial tensile tests are conducted on each structure after printing. The Trapezoid structure demonstrates superior load-bearing capability, sustaining loads above 85 N, while the U-Shape and T-Shape structures fail at loads below 70 N. The U-Shape structure's poor performance is attributed to weak interfacial binding, leading to delamination due to reliance solely on interlayer adhesion without sufficient consideration of interface geometry effects. Although the T-Shape structure incorporates interface geometry considerations, stress concentrations at the interface result in low strength.

Building on this, comparative experiments are conducted to validate the multi-material connection method and the MT-SEF (Mortise Tenon with Single Ellipse Filling) using RSR tensile specimens. With a fixed rigid plate setup, the mechanical properties of flexure hinges are evaluated, with results illustrated in **Fig. 3(b)**. These experiments assess tensile strength, ductility, and energy absorption of flexural hinges under different design parameters, aiming to optimize their application in multi-material connection structures.

We analyze the experimental results using four evaluation indicators: durability, versatility, performance-weight ratio, and parametric design. Regarding durability, we evaluate the lifespan and long-term performance of the connection through cyclic load testing. Faber et al. [39] printed rigid faces directly onto a rubber substrate, which resulted in interlayer delamination after limited folding cycles. Similarly, Wagner et al. [37] connected them by directly printing the hinges, encountering comparable delamination issues. We successfully addressed this issue by introducing an interlocking mechanism, which significantly enhanced the joint strength and improved its durability during the folding process. As for versatility, in addition to connection strength, the interlocking structure also introduces additional functionalities, such as energy absorption and impact resistance, thus expanding its application range. In terms of performance-to-weight ratio, we assess the ratio between structural strength or functionality and weight, which is particularly important for lightweight applications such as aerospace. As demonstrated in **Table 2**, the proposed method exhibits excellent mechanical properties while maintaining a lightweight design. When it comes to parametric design, by incorporating NPR method or other parametric design techniques, the performance of the interlocking structure can be enhanced, particularly in energy absorption. In our study, we parameterized the geometric factor ( $m$ ) of the ellipse, and by controlling parameters such as  $m$ , volume fraction, dimensions, and filling methods, we achieved programmable energy absorption and structural deformation properties. Although Ye et al. [34] achieved commendable mechanical properties, their approach primarily focused on material effects, neglecting structural contributions to overall performance. Other related studies similarly lacked parametric design strategies for optimizing structural performance. Our work fills these gaps by integrating a comprehensive parametric design framework that significantly enhances the interlocking method's efficacy.

**Table 2** compares the mechanical properties of various connection methods, where the proposed scheme exhibits better compatibility and mechanical performance. For instance, the structures provide excellent interlayer adhesion with viscoelastic materials and achieve high load-bearing capacity and durability under cyclic loads.

Under identical parameters, CSF, IPF, and solid filling (SF) are tested, with displacement-load curves shown in **Fig. 3(c)**. Analysis indicates that, while the SF structure performs best overall, CSF demonstrates superior energy absorption and ductility at loads below 200 N. As seen in **Fig. 3(d)**, under a constant load, the INPR-Connector with CSF exhibits significantly enhanced energy absorption and ductility compared to structures with IPF or SF. Specifically, CSF's energy absorption is 311.69% higher than IPF and 643.63% higher than SF at a fixed load of 150 N. This suggests that CSF not only absorbs more energy under load but also maintains better ductility at large displacements, thereby enhancing the structure's overall performance.

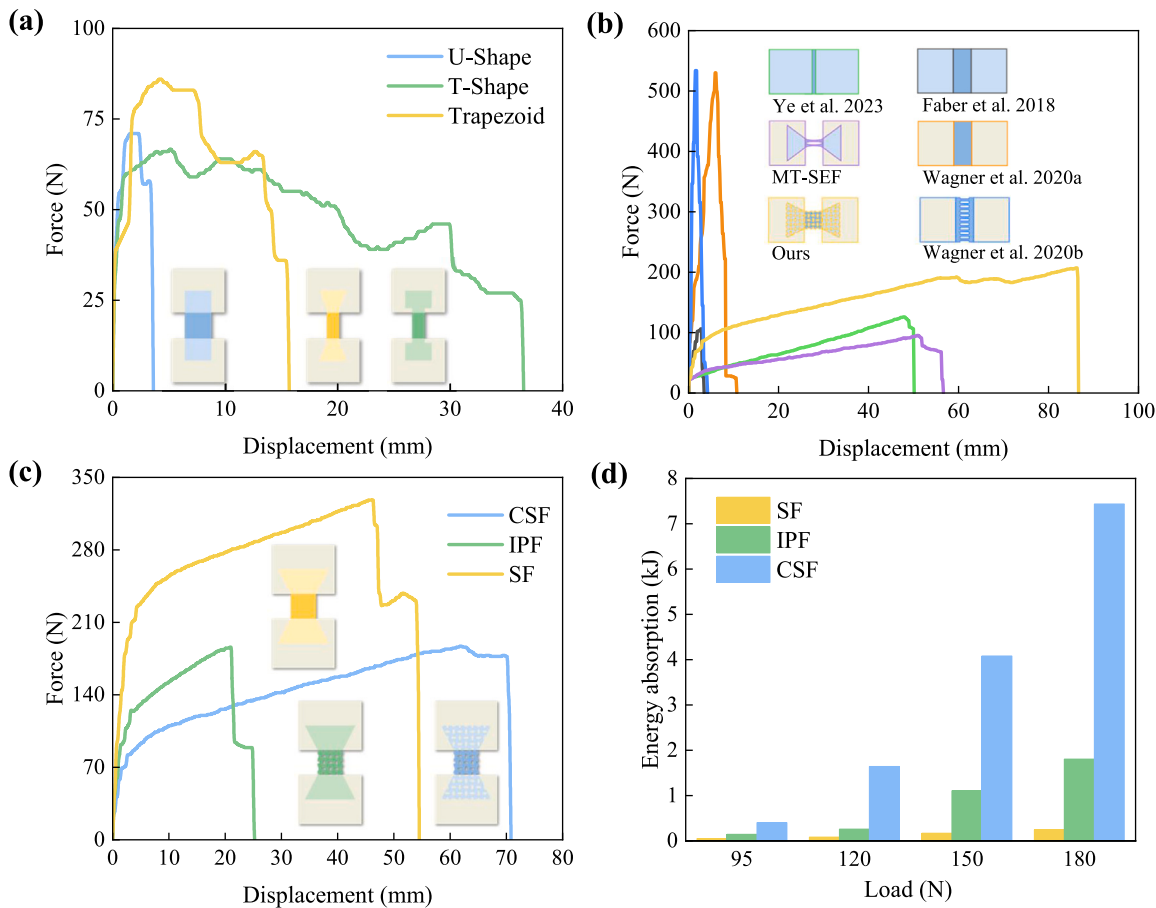


**Fig. 3.** Comparison of RSR connectors. (a) Traditional interlocking connection structures—U-Shape, T-Shape, and Trapezoid. (b) RSR structure from literature vs. our proposed structure. (c) Tensile test results for CSF, IPF, and SF under the same parameters. (d) Energy absorption of three structures under the same load.

**Table 2**  
Comparison of structural parameters for multi-material connection methods.

Method	Weight (g)	Ultimate load (N)	Fracture displacement (mm)	Fracture strain (%)	Specific ultimate load (N/g)
Faber et al. [39]	3.01	106	3.473	17.37	35.2
Wagner et al. [37]a	3.22	530	10.721	53.605	165
Wagner et al. [37]b	3.99	534	4.228	21.14	134
Ye et al. [34]	5.50	126	50.132	350.06	22.9
MT-SEF	2.45	95	56.625	157.29	39
Ours	1.99	207	86.674	433.37	104

#### 4.2. Simulation analysis for mechanical properties of connected structures

The Poisson's ratio of 2D NPR metamaterials is independent of their thickness. To optimize computational efficiency, finite element simulations are conducted on NPR cells with different geometric factors under equal thickness and minimum packing fraction constraints. For  $m = 1$ , the volume fractions are 25%, 45%, 65%, and 85%. For  $m = 2$  and  $m = 3$ , the volume fractions are 45%, 65%, and 85%. For  $m = 4$ , the volume fractions are 65% and 85%. Using the finite element software, the stress distribution is simulated for these INPR-Connectors under uniform horizontal displacement, as shown in Fig. 4.

Results indicate that, for a given geometric factor, higher volume fraction correspond to greater stress in the connected structure. For a fixed volume fraction, larger geometric factors (corresponding to larger void sizes) yield higher deformability and lower stress. This suggests that the INPR-Connector exhibits superior mechanical properties at a theoretical geometric factor of  $m = 4$  and volume fractions above the minimum of 49.8%, as calculated in Eq. (4). However, final mechanical properties should consider synthesized variables under manufacturable conditions.

Furthermore, it is observed that the stress distribution within the connection structure remains uniform across all volume fractions and geometric factors, with no significant stress concentration. Maximum stress decreases as the geometric factor increases, indicating that NPR structures improve performance due to their geometric characteristics and stress distribution behavior.

The analysis reveals that increasing cell wall thickness raises the critical tensile stress capacity, whereas increasing pore size reduces it. This demonstrates that wall thickness and pore size have opposing influences on the tensile strength of the structure. For a single cell with  $m = 1$ , only elements with thinner walls in the central region experience significant stretching under strain, while thicker-walled peripheral elements show greater resistance to tensile deformation. Consequently, the structure does not display the desired NPR effect.

Achieving a pronounced NPR effect requires a synergistic adjustment of wall thickness and pore size, so that wall thickness gradients and pore size gradients are properly matched. In such cases, elements within the structure progressively deform under strain, leading to the macroscopic NPR effect. Refer to Fig. 5 for further illustration.

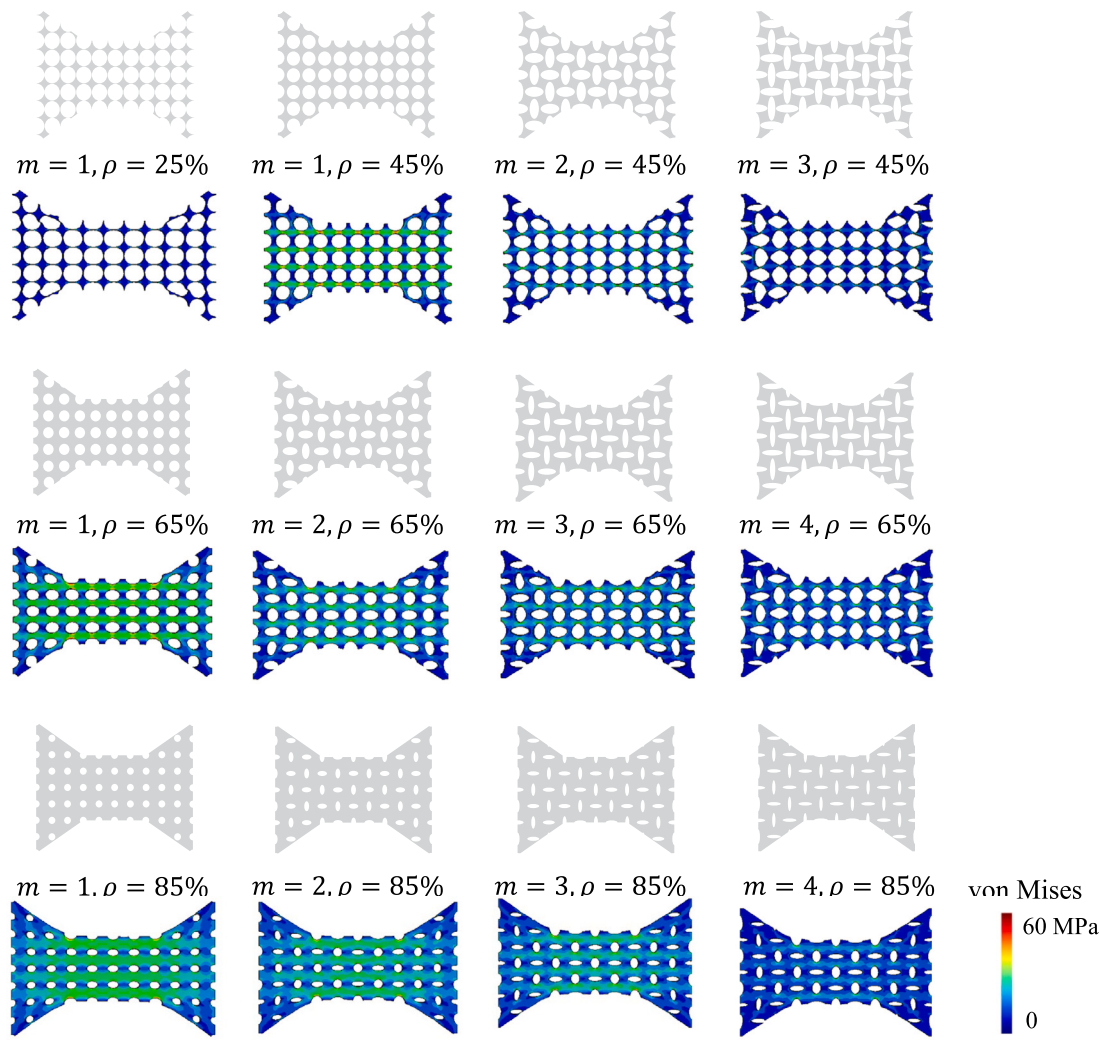


**Fig. 4.** Finite element analysis of INPR-Connector under four geometric factors with volume fractions of 25%, 45%, 65%, and 85%.

#### 4.3. Tensile test analysis of RSR samples

The NPR structure is integrated into the trapezoidal interlocking bulk material for the RSR samples, each with dimensions of 60 mm × 60 mm × 4 mm, and a hinge thickness of 2 mm. The details of the printed sample parts are provided in Section S1 of the Supplementary Materials. Tensile experiments are conducted on these samples using an MTS machine (10 kN load cell, USA) at a loading speed of 60 mm/min under ambient conditions.

This study examines the effect of geometric factors on the energy absorption capacity of RSR specimens with a volume fraction of 65%, maintaining a constant thickness of 2 mm for the connection structure. Two specimen types, each with dimensions 40 × 15 and 40 × 20, are tested. Figs. 6(a) and 6(b) depict the printing effects for the 40 × 15 samples, and Figs. 6(c) and 6(d) show those for 40 × 20 samples.

The tensile tests of these RSR samples highlight the fracture process and energy absorption effects. In the orthogonal elliptic NPR structure, the  $m$  of the ellipse significantly affects the Poisson's ratio and, consequently, the force-displacement curve. Through parametric analysis of the  $m$  value, the deformation characteristics of the structure can be tailored to specific needs. Smaller values of  $m$  generally result in smaller Poisson ratios, offering designs with less expansion during tension. And larger  $m$  values enhance the dilatation effect of the structure, leading to a more pronounced change in the force-displacement curve. The results indicate that the RSR sample with geometric factor  $m = 3$  achieves the best mechanical properties with CSF, owing to the dilatancy effect

of NPR structures during tension. Conversely, while  $m = 4$  exhibits favorable NPR characteristics, its performance is hindered by thinner cell walls. Although  $m = 1$  lacks NPR effects, its thicker walls improve overall mechanical performance.

The filling mode — either CSF or IPF — plays a critical role in shaping the force-displacement curve. CSF tends to produce more evenly distributed energy absorption, ideal for applications requiring consistent performance across the loading range. In contrast, IPF reduces the NPR effect during stretching, leading to a distinct force-displacement curve that prioritizes other mechanical properties, such as stiffness or localized strength. Both CSF and IPF display similar trends under tensile stress. However, IPF contributes less to tensile strength due to a smaller structural part, making its overall mechanical properties inferior to those of CSF.

Sample size also impacts mechanical properties. The 40 × 20 structure surpasses the 40 × 15 in energy absorption and ductility. The experimental results show that as the structure size increases, the energy absorption capacity also increases. This is because when the size of the unit cell is fixed, larger structures typically contain more units, which provides more space for deformation. Under applied load, the larger structure can distribute the force more efficiently across these additional units, thereby achieving a higher energy absorption effect, validating the effectiveness of this design in traditional block structures. Specimen fracture position [71,72] analysis is discussed in Section S2 of the Supplementary Materials, indicating that the designed interlocking structure has good performance.

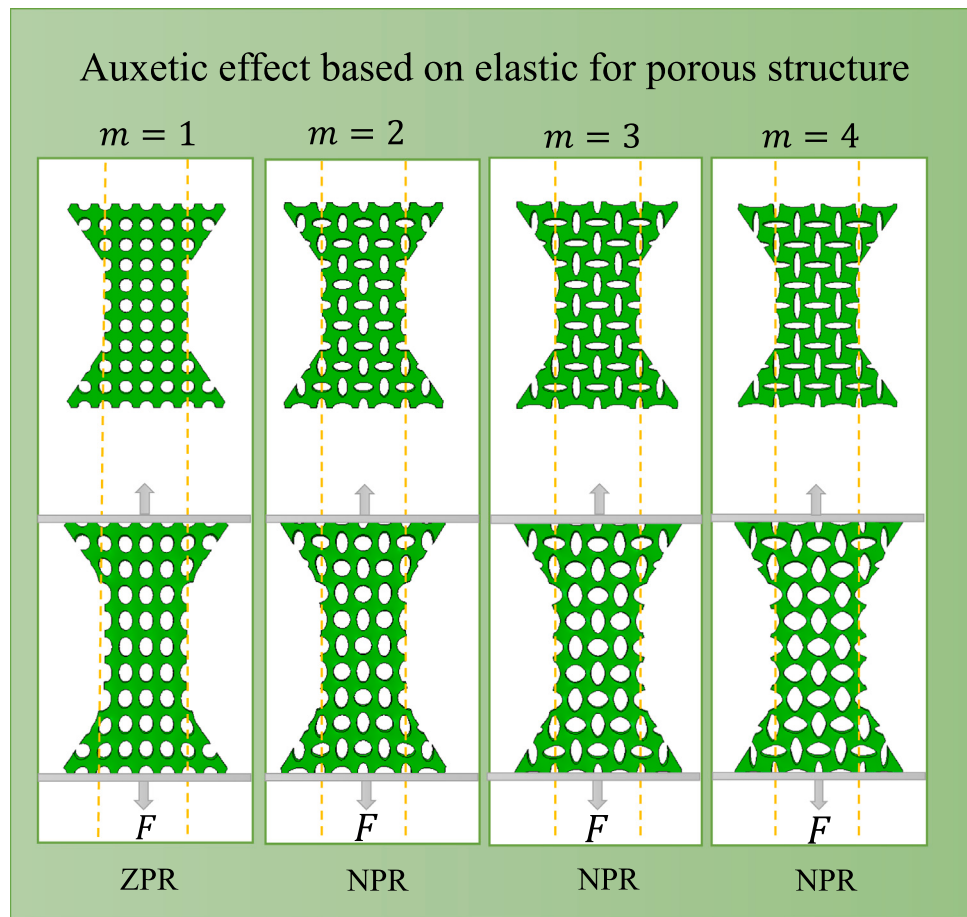


**Fig. 5.** The dilatancy effect of the connection structure under four geometric factors with a volume fraction of 65% is displayed.

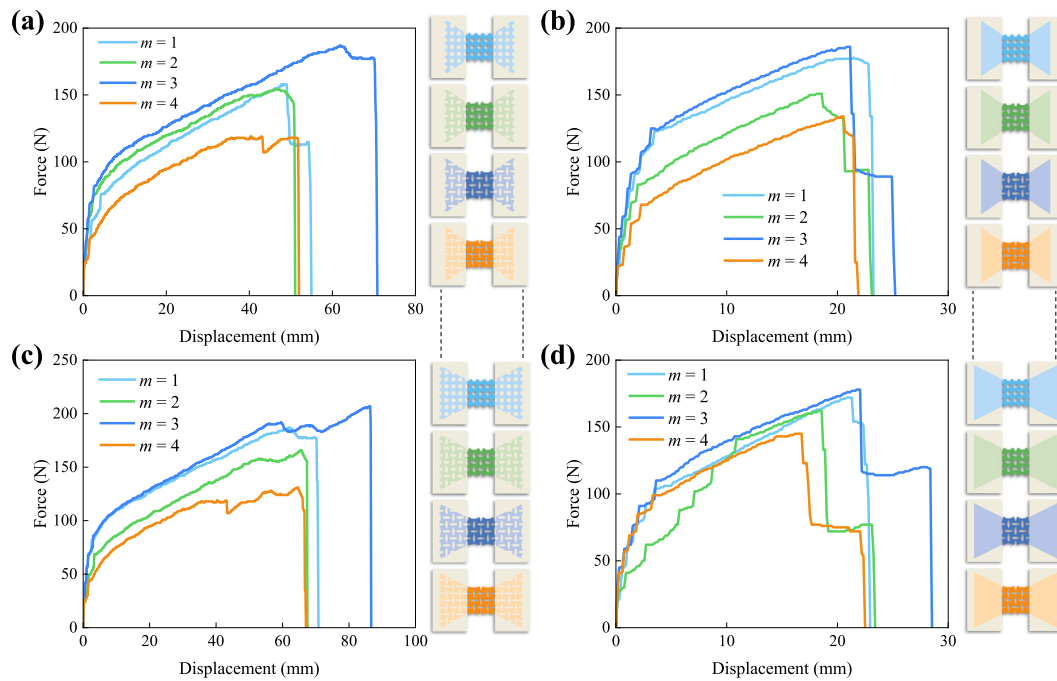


**Fig. 6.** Tensile test analysis of designed RSR samples. (a) CSF with lock size  $40 \times 15$ . (b) IPF with lock size  $40 \times 15$ . (c) CSF with lock size  $40 \times 20$ . (d) IPF with lock size  $40 \times 20$ .

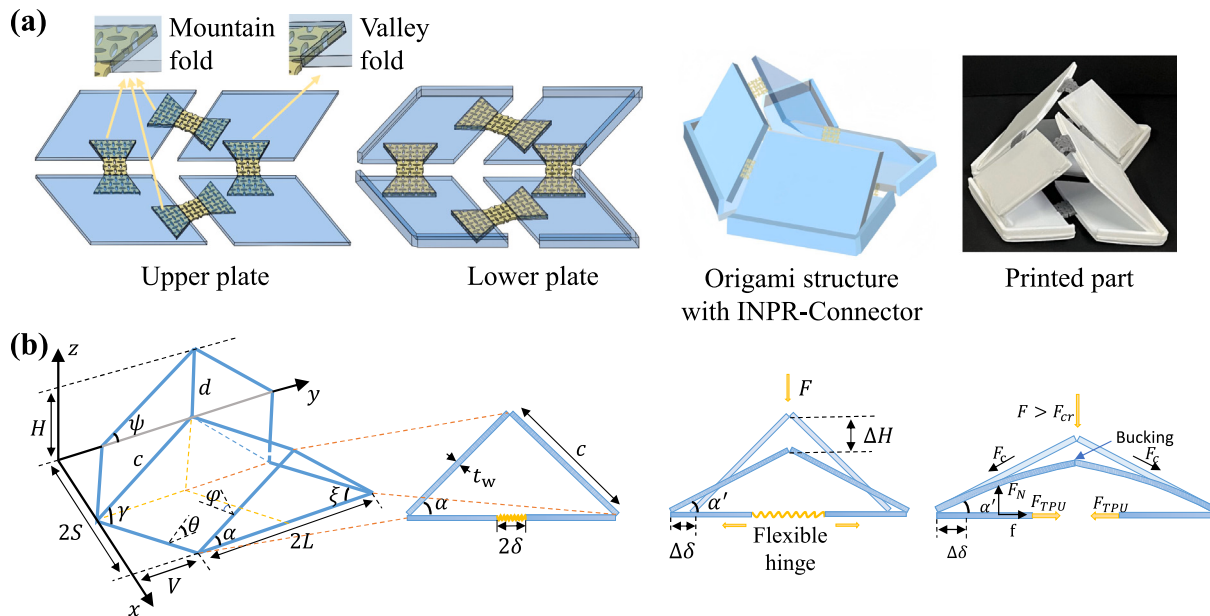


**Fig. 7.** Design and modeling of the INPR-Connector embedded origami structure. (a) Inset of the origami structure embedded INPR-Connector: upper and lower plate structure rendering, assembly simulation, and physical display of the printed origami structure embedded INPR-Connector. (b) Geometric framework and parameter analysis of the origami structure embedded INPR-Connector.

Research has demonstrated that orthogonal elliptical hole structures exhibit unique deformation patterns in different directions, enhancing impact resistance. These structures can promote localized buckling or shear deformation across multiple directions, thereby improving the durability and stability of materials under stress. By carefully adjusting the local geometric features of the material, the risk of overall failure is significantly reduced. Moreover, through geometric design, the auxetic structures enable a reduction in overall stiffness while preserving material strength, thereby optimizing stress distribution and facilitating efficient stress transfer within the structure. This approach results in improved mechanical performance and energy absorption capabilities. In this study, two INPR-Connectors were specifically designed for soft-hard interface connections. These connectors not only exhibit excellent mechanical properties but also significantly enhance the energy absorption capacity of the connected structure during deformation compared to conventional multi-material connections. Furthermore, these connectors remain intact and functional under repeated folding, demonstrating their superior durability and adaptability.

However, the proposed method has limitations. Excessively thin structural units may lower molding efficiency, and printing errors can occur due to extrusion delays and filament drag. Although pullback techniques and slower print speeds can reduce these issues, they may not fully eliminate them.

## 5. INPR-Connector embedded origami structure

In this paper, we combine a rigid plate with the INPR-Connector and apply it to an embedded origami unit composed of Miura origami, which can be regarded as bistable origami metamaterials. Specifically, we propose a flexible hinge variable origami structure with a rigid plate of adjustable thickness. This structure can be implemented in an origami framework that incorporates stretchable soft hinges. The hinge position, thickness, size, and the number of components can be adjusted according to specific design requirements.

As shown in Fig. 7(a), the upper and lower plates of the embedded origami unit are depicted. Two baffles are printed at each plate boundary of the lower plate to limit the movement of the upper plate. Bistability is achieved by folding the upper plate and fitting it into the baffles on the lower plate, forming an integrated embedded origami unit.

The origami structure embedded INPR-Connector is shown in Fig. 7(a), using a Miura crease pattern design. The Miura crease pattern exhibits bi-directional translation symmetry, comprising four congruent parallelograms arranged in a mosaic pattern. This geometry can be parameterized in several ways. For clarity, the origami cell is defined by the dimensions of its constituent parallelograms, with edge lengths  $c$  and  $d$ , and a sector angle  $\gamma$  as demonstrated in Fig. 7(b). The dihedral folding angle  $\theta \in [0, \pi/2]$  represents the angle between the facet and the  $xy$ -plane. Angles  $\xi$  and  $\psi$  represent the angles between the fold line and the  $y$ -axis, while  $\phi$  is the dihedral angle between the small plane and the  $yz$ -plane.

Since the height  $H$  between the upper and lower plates can be derived from the expression  $H = c \cdot \sin \gamma \cdot \sin \theta$  or  $H = c \cdot \sin \alpha$ , it follows that:

$$\sin \gamma \cdot \sin \theta = \sin \alpha. \quad (8)$$

After applying a force  $F$  to the top of the origami structure embedded INPR-Connector, the difference between the initial height and the height after compression deformation can be calculated as:

$$\Delta H = c \cdot (\sin \alpha - \sin \alpha'). \quad (9)$$

The vertical compressive force acting on the entire origami structure is transformed into tensile force along the horizontal soft hinges. During this process, the deformation of the soft hinge is expressed as:

$$\Delta \delta = c \cdot (\cos \alpha - \cos \alpha'). \quad (10)$$

When the applied force  $F$  exceeds the critical load  $F_{cr}$ , the upper plate begins to bend, and this critical force can be determined using the following equation:

$$F_{cr} = 4d \cdot \sigma_{cr} \cdot t_w \cdot \sin \alpha', \quad (11)$$

where  $\sigma_{cr}$  is the critical stress, which can be calculated according to the elastic/plastic theory of thick plates [73].

### 5.1. Quasi-static compression test of origami structure embedded INPR-connector with 2 × 2 elements

The soft hinges used in the experiments of this chapter adopt the INPR-Connector, as designed in the previous chapter. This paper analyzes the INPR-Connector filled with two different sizes and evaluates

**Table 3**

Eight geometric shape parameters under Structure I and Structure II.

Type	Joint dimension (mm)	c (mm)	$t_w$ (mm)	$\alpha$ ( $^{\circ}$ )	H (mm)
Structure I_1	7.5	50	4	36.8	30
Structure I_2	7.5	50	4	53.1	40
Structure I_3	7.5	50	4	66.9	46
Structure I_4	7.5	50	5	66.9	46
Structure II_1	10	50	4	36.8	30
Structure II_2	10	50	4	53.1	40
Structure II_3	10	50	4	66.9	46
Structure II_4	10	50	5	66.9	46

its performance as the intermediate soft hinge in the rigid plate of the origami structure. It also discusses the influence of the rigid plate's thickness. Two origami structures are designed, considering the size limitations of the printing platform.

Firstly, a soft hinge with a constant thickness and initial size of  $40 \times 15$  mm, reduced to  $20 \times 7.5$  mm, is used to form embedded folding Structure I, with a rigid plate thickness of  $t_w = 4$  mm and  $t_w = 5$  mm, respectively. Additionally, a soft hinge with an initial size of  $40 \times 20$  mm, reduced to  $20 \times 10$  mm, is used to form embedded folding Structure II, maintaining the same rigid plate thickness as Structure I. The effect of the trapezoidal joint size in the soft hinge, the thickness of the rigid plate, and the height  $H$  of the origami structure (which corresponds to the angle  $\alpha$ ) are investigated. The specific parameters are detailed in Table 3. These four origami structures are subjected to quasi-static compression tests using an MTS machine (10 kN load cell, USA) at room temperature, with a loading rate of 60 mm/min.

As shown in Figs. 8(a) and 8(b), during the compression process, the angle between the upper and lower plates decreases gradually. Part of the compressive force in the origami structure is converted into tensile force along the soft hinge of the lower plate. The results of the compression test are presented in Figs. 8(a) and 8(b), and the stress-strain curves for all types of origami structures are illustrated. The integral area under these curves represents the energy absorbed before failure.

Both Structure I and Structure II exhibit a transition from compressive force at the top to tensile force at the lower plate's soft hinge. Under strain conditions approaching 100%, the soft hinge remains intact, demonstrating the reliability and deformability of the designed connection structure.

Moreover, a thicker rigid plate ( $t_w$ ) significantly enhances the strength of the origami structure. Longer soft hinges can endure greater stretching and provide better energy absorption. Experimental results show that the primary deformation occurred in the soft hinges at the bottom, with maximum hinge extension exceeding 400%. The TPU soft hinges absorb significant energy during stretching and provide superior energy absorption without damage, even under higher compressive strains.

## 5.2. Energy absorption rate test

The energy absorption rate is directly related to the displacement-load area, and it can be controlled by designing an origami structure embedded INPR-Connector with varying geometric factors for the INPR-Connector under CSF and IPF. As shown in Fig. 8(c), when a rigid ball weighing 100 g is dropped from the same height, noticeable differences in the rebound height are observed, demonstrating the broad range of control over energy absorption. To enhance clarity, the position of the ball is outlined in the figure. Table 4 presents the average heights of the ball during each drop test, based on multiple trials.

The experimental results indicate that, due to structural and manufacturing constraints, the origami structure with a geometric factor of  $m = 3$  provides the best energy absorption, as evidenced by the lowest rebound height. Conversely, the energy absorption performance

**Table 4**

Ball fall and bounce heights at three moments for different geometric factors under CSF and IPF.

$\bar{H}_n$ (mm)	CSF $m = 1$	CSF $m = 2$	CSF $m = 3$	CSF $m = 4$	IPF
$\bar{H}_{t1}$	26	26	26	26	26
$\bar{H}_{t2}$	0	0	0	0	0
$\bar{H}_{t3}$	2.342	3.249	0.839	4.362	5.573

under IPF is comparatively inferior. For the connection structure with a geometric factor of  $m = 4$ , despite its favorable NPR characteristics, the thin wall thickness results in suboptimal energy absorption. In contrast, the structure with  $m = 1$  exhibits superior mechanical properties due to its thicker walls. This energy absorption trend is consistent with the tensile test results of the RSR samples.

We also explore the impact of the upper plate's connection method on the overall performance of the origami structure. As discussed in Section S3 of the Supplementary Materials, comparative experiments between SF and CSF-connected upper plates demonstrated that the CSF connection did not adversely affect the structure's mechanical performance.

## 5.3. Cyclic loading test of origami structure embedded INPR-Connector

A cyclic loading test is conducted on the origami structure embedded INPR-Connector, which consists of  $2 \times 2$  units. The structure is placed on the testing platform, with this position serving as the initial configuration for compression. The compression is applied at a rate of 60 mm/min. Detailed tests for all cases are provided in Section S4 of the Supplementary Materials. The load-unload behavior of the eight structures, as described in the previous section, is analyzed to observe the deformation patterns of the hinges for the two different sizes under varying plate parameters. These specific parameters are listed in Table 3. The maximum compressive z-axis strain reaches approximately 90%, and the full cyclic loading and unloading process for the origami structure embedded INPR-Connector is shown in Fig. 8(d).

During the compression phase, noticeable stretching of the soft hinge at the base of the origami structure is observed. Throughout the cyclic test, the peak force remains stable across each cycle, with no significant fluctuations or force decline detected, as shown in Fig. 8(d). This suggests that the origami structure embedded INPR-Connector can endure several loading cycles without failure. Additionally, the structure remains undamaged due to the soft hinge absorbing part of the applied energy during compression. Upon unloading, the origami structure is able to recover to its original shape, demonstrating its reusability.

## 6. Discussion

In this study, the NPR units of the INPR-Connector significantly enhance the energy absorption performance of the origami structure through the auxetic mechanism. When external load is applied to the structure, the NPR units first undergo deformation, with unit cells that have a larger aspect ratio showing significant auxetic effects under compression. This auxetic mechanism not only absorbs energy effectively through geometric interlocking, preventing excessive energy concentration or local failure, but also allows the structure to recover its shape after repeated loading while maintaining excellent mechanical properties. By incorporating the design of bistable origami structure embedded with INPR-Connector, this mechanism is further optimized, resulting in higher energy absorption efficiency and greater stability under various loading conditions. This validates the system's superior impact resistance under dynamic loads.

In this work, the material used plays a crucial role in energy absorption performance. The mechanical properties of different materials, such as elastic modulus, yield strength, and plastic deformation

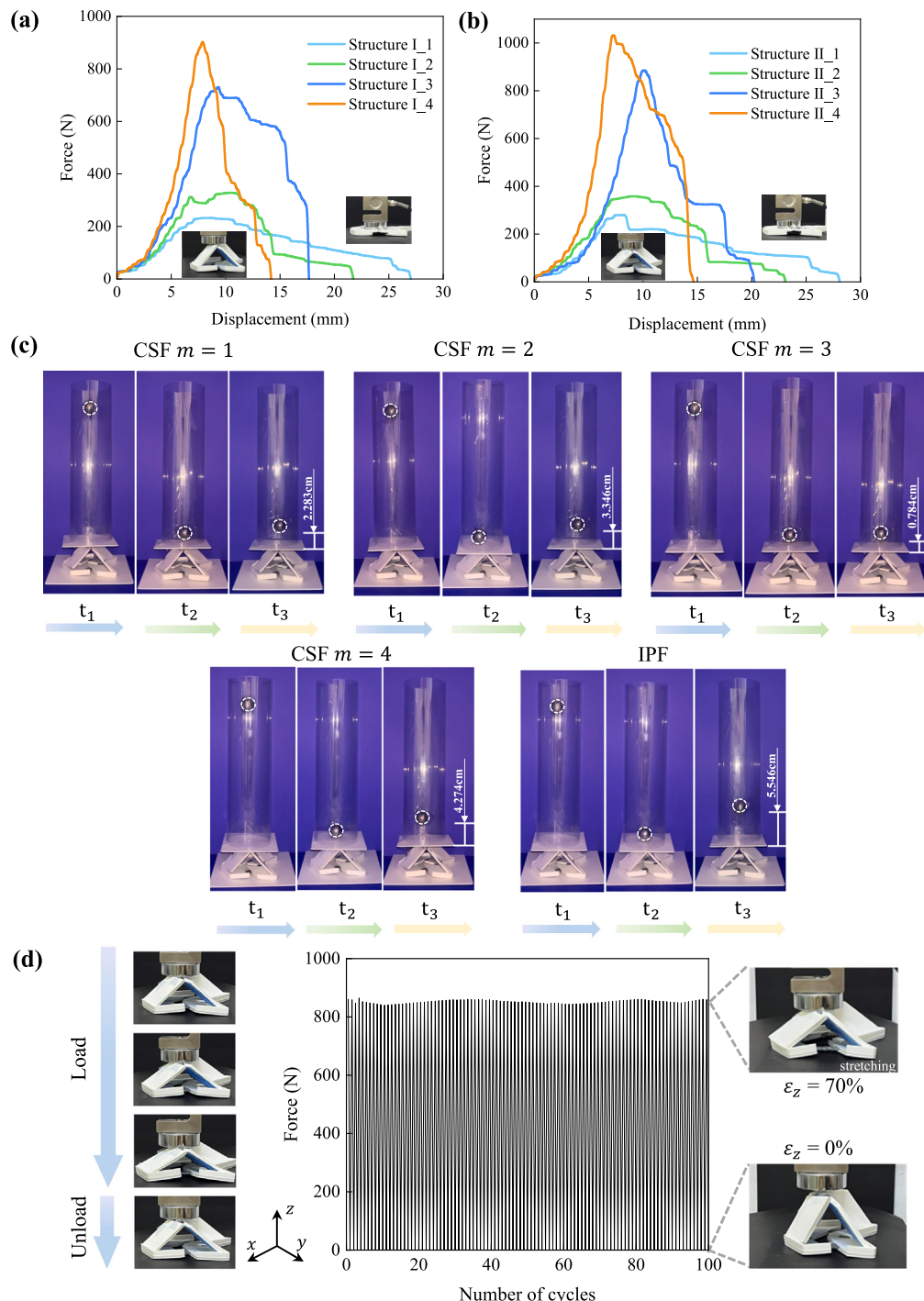


**Fig. 8.** Experiment for origami structure embedded INPR-Connector. (a) Compression load–displacement curves of four origami structures under Structure I. (b) Compression load–displacement curves of four origami structures under Structure II. (c) Adjustable and controllable energy absorption rate of INPR-Connector under embedded origami structure. (d) Cyclic compression test of an origami structure embedded INPR-Connector with  $2 \times 2$  elements.

capacity, directly influence how the structure deforms under load and how energy is absorbed. Given the unique characteristics of NPR structures, selecting materials with good plasticity and ductility is particularly important. For example, TPU exhibits excellent elasticity and plasticity, allowing it to maintain high energy absorption efficiency even during large deformations. Its hardness also significantly affects its performance. Low-stiffness TPU has high elongation and elasticity, making it suitable for applications that require flexibility and impact resistance, although it has poor tensile strength and wear resistance. Conversely, high-stiffness TPU offers better tensile strength and wear

resistance, making it ideal for high-strength loading and wear-resistant applications, but it has lower elongation and is more brittle. The choice of TPU stiffness should strike a balance between flexibility, strength, and durability, depending on the specific application requirements.

The connection mode of NPR structure has an important influence on its mechanical properties and energy absorption capacity. In terms of energy absorption, the method proposed in this paper, the proposed method shows significant improvement compared to the methods of Faber et al. [39] and Wagner et al. b [37]. Specifically, the energy absorption capacity of the Wagner et al. a [37] method was increased

to 428% by our method, meanwhile, Ye et al. [34] and the MF-SEF methods were improved to 261% and 282% using our method, respectively. These results highlight the clear advantage of our method in energy absorption performance, confirming its potential for efficient energy absorption design. In this study, an alternating elliptical NPR structure was used. By parameterizing the elliptical holes and considering two different unit cell quantities (CSF and IPF), the impact of varying  $m$  on the energy absorption performance of these two structures was analyzed. It was found that CSF exhibits better energy absorption performance compared to IPF. The alternating elliptical NPR structure with  $m = 4$  shows the best NPR effect, which aligns with the NPR effects observed in both the simulation and physical experiments.

The origami structure proposed in this study has significant engineering application potential, particularly in fields that require efficient energy absorption. For example, the origami structure can be used as a cushioning layer in automotive hoods and helmets, functioning as a sandwich structure. In this context, the soft hinges during deformation absorb energy, helping to mitigate impact forces on children's heads in vehicle collisions while providing cushioning [74]. Additionally, it can be applied in aerospace, such as in deployable structures for satellite solar panels, antennas, and detection equipment, as well as in vibration damping systems. In these applications, the structure must not only possess excellent energy absorption capabilities but also ensure stability, reusability, and long-term material durability.

## 7. Conclusion

This paper proposes a design method for INPR-Connector, focusing on the NPR effect and energy absorption of the connectors. Unlike conventional methods, we not only address challenges associated with connection joints but also explore the influence of the filling structure on the mechanical performance of the connectors. The novelty of this method lies in employing a mortise-and-tenon (interlocking) structure to connect geometric interfaces connections, thereby significantly enhancing joint strength. Additionally, we incorporate an orthogonal elliptical hole structure with excellent energy absorption and vibration damping properties. This structure is parameterized to maintain superior energy absorption performance while ensuring compatibility with deployable systems. Moreover, we demonstrate the integration of the INPR-Connector with a rigid plate to construct a deployable bistable origami structure inspired by origami principles. By controlling the structural angles, we achieve tunable energy absorption, showcasing the feasibility and versatility of the proposed connector design. These innovations collectively provide a new perspective on advanced connector systems, offering improved mechanical performance and multifunctionality.

The wall thickness of the filled unit cell and the manufacturing process significantly influence the stability and strength of the structure. In future work, we will focus on topology optimization based on stress distribution to mitigate strain localization within the connection structure. This will aim to enhance the uniformity of deformation and reduce localized stress concentrations. Moreover, the incorporation of filler materials, such as short fibers or nanoparticles, will be explored as a means of dispersing local stresses effectively. To address material anisotropy, we plan to optimize the printing paths [75,76] to ensure that the material deposition direction aligns with anticipated load paths. This alignment will reduce the effects of anisotropy and significantly enhance the mechanical performance of the structure. These strategies will not only improve the performance of the connection structure but also provide a foundation for designing high-performance structures suitable for diverse mechanical environments and application requirements. The multi-material additive manufacturing approach demonstrated in this study paves the way for the development of deployable structures with exceptional adaptability and reliability, offering broad application prospects.

## CRediT authorship contribution statement

**Wenpeng Xu:** Writing – review & editing, Writing – original draft, Validation, Supervision, Resources, Methodology, Investigation, Funding acquisition, Formal analysis, Conceptualization. **Mengyu Zhang:** Writing – review & editing, Writing – original draft, Visualization, Validation, Formal analysis, Data curation. **Hao Xu:** Writing – review & editing, Writing – original draft, Visualization, Validation, Investigation, Formal analysis, Data curation. **Menglin Yu:** Writing – original draft, Investigation, Formal analysis, Data curation. **Liuchao Jin:** Writing – review & editing, Writing – original draft, Visualization, Validation, Methodology, Investigation, Formal analysis, Data curation, Conceptualization. **Xiaoya Zhai:** Writing – review & editing, Writing – original draft, Validation, Supervision, Methodology, Funding acquisition, Formal analysis, Conceptualization. **Jingchao Jiang:** Writing – review & editing, Writing – original draft, Visualization, Validation, Supervision, Methodology, Investigation, Conceptualization.

## Declaration of competing interest

The authors declare that they have no known competing financial interests or personal relationships that could have appeared to influence the work reported in this paper.

## Acknowledgments

This work is supported by the Provincial Natural Science Foundation of Henan General Program (No. 242300420281), the Fundamental Research Funds for the Universities of Henan Province (No. NSFRF240817), the National Natural Science Foundation of China (No. 62402467, No. 61972368, No. 12371383), the Youth Innovation Key Research Funds for the Central Universities, China (No. YD0010002010), the Strategic Priority Research Program of the Chinese Academy of Sciences, China (No. XDB0640000), and the National Key R&D Program of China (No. 2024YFA1016300). For open access, the author has applied a 'Creative Commons Attribution (CC BY) license to any Author Accepted Manuscript version arising from this submission.

## Appendix A. Supplementary data

Supplementary material related to this article can be found online at <https://doi.org/10.1016/j.compositesb.2025.112243>.

## Data availability

The authors confirm that the data supporting the findings of this study are available within the article.

## References

- [1] Wang W, Rodrigue H, Ahn S-H. Deployable soft composite structures. *Sci Rep* 2016;6(1):20869.
- [2] Jin L, Li B, Tian D, Wang Q, Hou Y. Impact dynamic response of large aperture space deployable antenna supporting structures based on a dual-scale model. *Thin-Walled Struct* 2024;195:111432.
- [3] Zhang J, Lu G, Zhang Y, You Z. A study on ballistic performance of origami sandwich panels. *Int J Impact Eng* 2021;156:103925.
- [4] Liu T, Huang J, Yan S, Guo F. Extraction and analysis of transient signals of a deployable structure vibration based on the sparse decomposition with mixed norms. *Aerospace Sci Technol* 2020;105:106064.
- [5] Zeng C, Liu L, Bian W, Leng J, Liu Y. Compression behavior and energy absorption of 3D printed continuous fiber reinforced composite honeycomb structures with shape memory effects. *Addit Manuf* 2021;38:101842.
- [6] Xiao Y, Hu HL, Wang YJ, Long H, Liu Y, Wu Q. Energy absorption characteristics of origami-folded thin-walled square tubes internally filled with graded polyurethane foam structures. *Mech Adv Mater Struct* 2024;1–16.
- [7] Khazaaleh S, Dalaq AS, Daqaq MF. An origami-inspired energy absorber. *Smart Mater Struct* 2024;33(4):045029.

- [8] Xing S, Jiang Z, Zhao J, Sun X, Wang Y. Failure mechanism and crashworthiness optimization of variable stiffness nested origami crash box. *Eng Fail Anal* 2024;108953.
- [9] Chen Y, Deng X, Huang H. Crashworthiness of multicellular tubes under axial compression based on polygonal origami folding. *J Eng Mech* 2024;150(12):04024085.
- [10] Zhu Y, Filipov ET. Large-scale modular and uniformly thick origami-inspired adaptable and load-carrying structures. *Nat Commun* 2024;15(1):2353.
- [11] Fan Z, Wang R, Huang H, Li X. Design and analysis of an origami-inspired modular thick-panel deployable structure. *Int J Mech Sci* 2024;282:109579.
- [12] Liu X, Zhang K, Shi H, Hong F, Liu H, Deng Z. Origami-inspired metamaterial with compression-twist coupling effect for low-frequency vibration isolation. *Mech Syst Signal Process* 2024;208:111076.
- [13] Wang C, Zhang D, Li J, Li Y, Zhang X. Deployment dynamics of thick panel Miura-origami. *Aerospace Sci Technol* 2024;144:108795.
- [14] Shi H, Zhang K, Liu X, Liu H, Peng H, Deng Z. Vibration suppression of a meta-structure by hybridization of Kresling origami and waterbomb-based origami. *Compos Struct* 2024;334:117964.
- [15] Shi P, Chen Y, Wei J, Xie T, Feng J, Sareh P. Design and low-velocity impact behavior of an origami-bellow foldcore honeycomb acoustic metastructure. *Thin-Walled Struct* 2024;197:111607.
- [16] Cui Z, Qi J, Tie Y, Zou T, Duan Y. Research on the energy absorption properties of origami-based honeycombs. *Thin-Walled Struct* 2023;184:110520.
- [17] Liu X, Zhang Y, Su Y, Geng C, Liu Y, He J, et al. 4D printing of cellular silicones with negative stiffness effect for enhanced energy absorption and impact protection. *Compos Part B: Eng* 2024;282:111561.
- [18] Zhu K, Zheng X, Peng J, Sun J, Huang R, Yan L. The relationship between the impact position interference and CAI strength of composite sandwich structures under double impacts. *Compos Part B: Eng* 2024;268:111092.
- [19] Zhou Y, Jiang D, Wang L, Xiang P, Jia L-J. Cushioning performance of origami negative Poisson's ratio honeycomb steel structure. *Thin-Walled Struct* 2024;204:112284.
- [20] Qiang W, Durandet Y, Zhang X, Lu G. Experimental and numerical study on energy absorption performance of truncated origami materials. *Thin-Walled Struct* 2024;200:111911.
- [21] Xue W, Sun Z, Ye H, Liu Q, Jian B, Wang Y, et al. Rigid-flexible coupled origami robots via multimaterial 3D printing. *Smart Mater Struct* 2024;33(3):035004.
- [22] Cha J-H, Kumar SKS, Jang W-H, Lee H, Kim JG, Park G, et al. Multidisciplinary space shield origami composite: Incorporating cosmic radiation shielding, space debris impact protection, solar radiative heat shielding, and atomic oxygen erosion resistance. *Compos Part B: Eng* 2025;288:111876.
- [23] Schlothauer A, Fasel U, Keidel D, Ermanni P. High load carrying structures made from folded composite materials. *Compos Struct* 2020;250:112612.
- [24] Mallesh S, Kim M, Seok C, Hong D-J, Kim M, Hyun J, et al. Folded-core radar-absorbing sandwich composite with sendust particle-added Ni-plated glass/polyether ether ketone thermoplastic resin in the ultrahigh-frequency band. *Compos Part B: Eng* 2023;264:110921.
- [25] Darnal A, Mantri K, Betts W, Kalantar N, Kim J, Muliana A. Flexibility, toughness, and load bearing of 3D-printed chiral kerf composite structures. *Compos Part B: Eng* 2024;284:111685.
- [26] Butler R. Academic research for composite aerostructures-A personal perspective. *Compos Part B: Eng* 2024;273:111239.
- [27] Shah SIH, Bashir S, Ashfaq M, Altaf A, Rmili H. Lightweight and low-cost deployable origami antennas—A review. *IEEE Access* 2021;9:86429–48.
- [28] Lappas V, Adeli N, Visagie L, Fernandez J, Theodorou T, Steyn W, et al. CubeSail: A low cost CubeSat based solar sail demonstration mission. *Adv Space Res* 2011;48(11):1890–901.
- [29] Gruber P, Häuplik S, Imhof B, Özdemir K, Waclavicek R, Perino MA. Deployable structures for a human lunar base. *Acta Astronaut* 2007;61(1–6):484–95.
- [30] Wang Q, Li S, Liu Z, Wu G, Lei J, Wang Z. Geometric design and energy absorption of a new deployable cylinder tube. *Mech Adv Mater Struct* 2022;29(13):1911–24.
- [31] Wo Z, Ranezes JM, Filipov ET. Locking zipper-coupled origami tubes for deployable energy absorption. *J Mech Robot* 2022;14(4):041007.
- [32] Wu C, Zhao P, Chang Z, Li L, Zhang D. An experimental and numerical investigation of ballistic penetration behaviors of deployable composite shells. *Acta Astronaut* 2024;224:533–45.
- [33] Deleo AA, O'Neil J, Yasuda H, Salvatiato M, Yang J. Origami-based deployable structures made of carbon fiber reinforced polymer composites. *Compos Sci Technol* 2020;191:108060.
- [34] Ye H, Liu Q, Cheng J, Li H, Jian B, Wang R, et al. Multimaterial 3D printed self-locking thick-panel origami metamaterials. *Nat Commun* 2023;14(1):1607.
- [35] Chueh Y-H, Zhang X, Wei C, Sun Z, Li L. Additive manufacturing of polymer-metal/ceramic functionally graded composite components via multiple material laser powder bed fusion. *J Manuf Sci Eng* 2020;142(5):051003.
- [36] Chueh Y-H, Wei C, Zhang X, Li L. Integrated laser-based powder bed fusion and fused filament fabrication for three-dimensional printing of hybrid metal/polymer objects. *Addit Manuf* 2020;31:100928.
- [37] Wagner MA, Huang J-L, Okle P, Paik J, Spolenak R. Hinges for origami-inspired structures by multimaterial additive manufacturing. *Mater Des* 2020;191:108643.
- [38] Hunter C, Vijayachandran A, Waas AM. Self-deployable hinges for monolithic space structures using multi-material additive manufacturing. *Acta Astronaut* 2024;214:641–9.
- [39] Faber JA, Arrieta AF, Studart AR. Bioinspired spring origami. *Science* 2018;359(6382):1386–91.
- [40] Adib AZ, Pratama J, Badranaya MI, Mahardika M, Suyitno, Salim UA, Arifvianto B. Flexural strength of the sandwich-structured parts made of polylactic-acid and thermoplastic-polyurethane fabricated by using extrusion-based multi-material additive manufacturing. *Int J Adv Manuf Technol* 2024;132:4805–27.
- [41] Kakaraparthi S, Chen N. A multi-material additive manufacturing virtual prototyping method for design to improve part strength. *Int J Adv Manuf Technol* 2023;127(3):1505–16.
- [42] Cunha P, Teixeira R, Carneiro O, Silva A. Multi-material fused filament fabrication: an expedited methodology to assess the affinity between different materials. *Prog Addit Manuf* 2023;8(2):195–204.
- [43] Yang H, Jiang W, Li M, Ma L. Multi-material 3D double-V metastructures with tailororable Poisson's ratio and thermal expansion. *Int J Mech Sci* 2021;210:106733.
- [44] Ituarte IF, Boddeti N, Hassani V, Dunn ML, Rosen DW. Design and additive manufacture of functionally graded structures based on digital materials. *Addit Manuf* 2019;30:100839.
- [45] Brischetto S, Ferro CG, Torre R, Maggiore P. 3D FDM production and mechanical behavior of polymeric sandwich specimens embedding classical and honeycomb cores. *Curved Layer Struct* 2018;5(1):80–94.
- [46] Saldivar M, Tay E, Isaakidou A, Moosabeiki V, Fratila-Apachitei L, Doubrovski E, et al. Bioinspired rational design of bi-material 3D printed soft-hard interfaces. *Nat Commun* 2023;14(1):7919.
- [47] Porter MM, Ravikumar N, Barthelat F, Martini R. 3D-printing and mechanics of bio-inspired articulated and multi-material structures. *J Mech Behav Biomed Mater* 2017;73:114–26.
- [48] Stano G, Ovy SAI, Percoco G, Zhang R, Lu H, Tadesse Y. Additive manufacturing for bioinspired structures: experimental study to improve the multimaterial adhesion between soft and stiff materials. *3D Print Addit Manuf* 2023;10(5):1080–9.
- [49] Xia L, Bi M, Wu J, Wang F, Wang L, Xie YM, et al. Integrated lightweight design method via structural optimization and path planning for material extrusion. *Addit Manuf* 2023;62:103387.
- [50] Cao A, Wan D, Gao C, Elverum CW. A novel method of fabricating designable polylactic acid (PLA)/thermoplastic polyurethane (TPU) composite filaments and structures by material extrusion additive manufacturing. *J Manuf Process* 2024;118:432–47.
- [51] Fu T, Hu X, Yang C. Impact response analysis of stiffened sandwich functionally graded porous materials doubly-curved shell with re-entrant honeycomb auxetic core. *Appl Math Model* 2023;124:553–75.
- [52] Fu T, Rao E, Rabczuk T. Sound transmission loss and energy absorbing performance of stiffened doubly-curved shells with corrugated-honeycomb hybrid cores. *Eur J Mech A Solids* 2024;107:105386.
- [53] Yu Y, Fu T, Wang S, Yang C. Dynamic response of novel sandwich structures with 3D sinusoid-parallel-hybrid honeycomb auxetic cores: The cores based on negative Poisson's ratio of elastic jump. *Eur J Mech A Solids* 2025;109:105449.
- [54] He Y, Zhang P, You Z, Li Z, Wang Z, Shu X. Programming mechanical metamaterials using origami tessellations. *Compos Sci Technol* 2020;189:108015.
- [55] Balan M, Mertens J, Bahubalendruni MR. Auxetic mechanical metamaterials and their futuristic developments: A state-of-art review. *Mater Today Commun* 2023;34:105285.
- [56] Lim T-C. A mechanical metamaterial with adjustable positive to negative Poisson's ratio based on rotating trapeziums and triangles. *Phil Mag* 2024;104(5):300–20.
- [57] Wang H, Nie R, Zhang C, Ji H, Qiu J. Investigation of bi-directional re-entrant anti-tetrachiral structure for regulating negative Poisson's ratio. *Mech Adv Mater Struct* 2023;1–16.
- [58] Feng N, Tie Y, Guo R, Yuan Q, Xue F, Li C, et al. A concave four-arc honeycomb with enhanced stiffness and desirable negative Poisson's effect. *Sci Rep* 2023;13(1):21144.
- [59] Yang L, Ye M, Huang Y, Dong J. Mechanics characteristics of a 3D star-shaped negative Poisson's ratio composite structure. *Materials* 2023;16(11):3950.
- [60] Qin S, Deng X, Yang F, Lu Q. Energy absorption characteristics and negative Poisson's ratio effect of axisymmetric tetrachiral honeycombs under in-plane impact. *Compos Struct* 2023;323:117493.
- [61] Li S, Li B, Fu T. Low-velocity impact response of sandwich plates with corrugation star-shaped honeycomb hybrid core. *Appl Math Model* 2025;137:115715.
- [62] Wang X, Fu T. A novel arc-type auxetic cellular doubly-curved shells with negative Poisson's ratio for broadband low-frequency sound insulation. *Eur J Mech A Solids* 2024;106:105326.
- [63] Fu T, Wang X, Rabczuk T. Broadband low-frequency sound insulation of stiffened sandwich PFGM doubly-curved shells with positive, negative and zero Poisson's ratio cellular cores. *Aerospace Sci Technol* 2024;147:109049.

- [64] Moradweysi P, Santucci P, Carta G, Goudarzi T, Aghdam M, Baldi A, et al. Design and analysis of a thick miura-ori folded structure with large negative Poisson's ratio. *Mech Adv Mater Struct* 2024;31(4):908–26.
- [65] Ma Y, Liu Z, Zhang T, Li S, Lei J. Crushing behavior and energy absorption performance of a novel 3D folded structure with negative Poisson's ratio. *Adv Eng Mater* 2023;25(10):2201769.
- [66] Pagliocca N, Uddin KZ, Anni IA, Shen C, Youssef G, Koohbor B. Flexible planar metamaterials with tunable Poisson's ratios. *Mater Des* 2022;215:110446.
- [67] Wang H, Xiao S-H, Zhang C. Novel planar auxetic metamaterial perforated with orthogonally aligned oval-shaped holes and machine learning solutions. *Adv Eng Mater* 2021;23(7):2100102.
- [68] Robert F. An isotropic three-dimensional structure with Poisson's ratio = -1. *J Elasticity* 1985;15(4):427–30.
- [69] Larsen UD, Signund O, Bouwsta S. Design and fabrication of compliant micromechanisms and structures with negative Poisson's ratio. *J Microelectromech Syst* 1997;6(2):99–106.
- [70] Grima JN, Gatt R, Alderson A, Evans K. On the potential of connected stars as auxetic systems. *Mol Simul* 2005;31(13):925–35.
- [71] Khosravani MR, Božić Ž, Zolfagharian A, Reinicke T. Failure analysis of 3D-printed PLA components: Impact of manufacturing defects and thermal ageing. *Eng Fail Anal* 2022;136:106214.
- [72] Khosravani MR, Zolfagharian A. Fracture and load-carrying capacity of 3D-printed cracked components. *Extrem Mech Lett* 2020;37:100692.
- [73] Wang C, Xiang Y, Chakrabarty J. Elastic/plastic buckling of thick plates. *Int J Solids Struct* 2001;38(48–49):8617–40.
- [74] Zou T, Chen D, Li Q, Wang G, Gu C. A novel straw structure sandwich hood with regular deformation diffusion mode. *Compos Struct* 2024;337:118077.
- [75] Xu W, Xu H, Zhai X, Jiang J. Nature-inspired interlaced printing strategies for additive manufacturing highly improved mechanical properties. *Addit Manuf* 2024;89:104276.
- [76] Xu W, Xu H, Li Q, Zhang P, Yang L, Wang W. Stress-based continuous planar path planning for additive manufacturing. *Adv Eng Softw* 2024;188:103544.